Tilted-potential photonic crystal cavities for integrated quantum photonics

A. DELGOFFE,[*] A. MIRANDA, B. RIGAL, A. LYASOTA, A. RUDRA, B. DWIR, AND E. KAPON

Ecole Polytechnique Fédérale de Lausanne (EPFL), CH–1015 Lausanne, Switzerland
[*]*antoine.delgoffe@epfl.ch*

Abstract: We propose and investigate a new type of photonic crystal (PhC) cavity for integrated quantum photonics, which provides tailored optical modes with both confined and extended spatial components. The structures consist of elongated PhC cavities in which the effective index of refraction is varied quasi-linearly along their axis, implemented by systematic lateral shifts of the PhC holes. The confined modes have approximately Airy-function envelopes, exhibiting single peaks and extended tails, which is useful for optimizing single photon extraction and transmission in integrated quantum photonic devices. The measured spectrally resolved near-field patterns of such devices show the expected spatial and resonance wavelength behavior, in agreement with numerical simulations of the Airy-Bloch modes. The effects of fabrication-induced disorder on the mode features are also analyzed and discussed. Selective excitation of specific Airy-Bloch modes using integrated, site-controlled quantum dots as localized light sources is demonstrated. Based on the tilted-potential cavity, multiple-QD single photon emitters exploiting wavelength division multiplexing are proposed.

1. Introduction

Tailoring the features of photonic confinement in nanostructures provides means for adjusting the spectral and local density of states of electromagnetic modes. Such adjustments are useful for tailoring the optical interaction of atoms, molecules and solid-state nanostructures embedded in the modified photonic environment. For example, placing semiconductor quantum dots (QDs) in nano-photonic cavities of small mode volume and high Q-factors is useful for efficient extraction of single photons emitted by the QDs, enhanced by the Purcell effect [1]. Coupling of QDs to photonic waveguides, on the other hand, enables single photon transport over macroscopic distances [2], which can be exploited for qubit transmission in quantum networks [3]. More generally, integration of QDs with specific configuration of photonic cavities and waveguides is being explored for the realization of integrated quantum photonic circuits, for producing, manipulating and detecting single photons on-chip [4–9].

The dual goal of efficient single photon extraction from the light emitter and its subsequent transport to a prescribed destination on the chip requires opposing features of the confined photonic mode. Whereas efficient extraction exploiting the Purcell effect benefits from a highly confined mode, photon transport necessitates the use of extended photonic modes. An optimal design of a single photon source on-chip thus involves the optimization of the spatially localized and extended aspects of the photonic modes employed. One approach towards this goal has been the integration of coupled cavity-waveguide structures implemented in a photonic crystal (PhC) membrane system [10,11]. Optimizing the optical coupling between the cavity and the waveguide and avoiding mode localization due to disorder can yield efficient single photon "injectors" for in-plane photonic integration [12,13].

In the present work we propose and demonstrate a new type of PhC cavity supporting modes with specifically tailored spatial distributions of intensity. The cavities exhibit linear effective

mode index variation along their axis, yielding Airy-function-like near field envelope functions, analogous of confined particle states in triangular-potential quantum wells. The resulting Airy-Bloch modes are highly localized at prescribed locations along the cavity, but exhibit extended tails across its entire length, which makes them suitable for single photon extraction and transport when used with properly positioned QDs. The effect of fabrication-induced disorder on the mode structure is also discussed. Selective excitation of specific Airy-Bloch modes using site-controlled pyramidal QDs is demonstrated as a first step towards making efficient single photon injectors for integrated quantum photonics.

2. Concept

The tailored-index structures are derived from long L_n PhC membrane cavities (membrane effective index $n_{eff.}^{slab}$) in which the effective mode index $n_{eff.}^{mode}$ of an otherwise uniform cavity (or W1 waveguide) is varied quasi-linearly along the cavity axis (see Fig. 1). A missing row of holes in the triangular PhC lattice defines the axis of the long cavity. The first rows of PhC holes on both sides of this defect are shifted outwards by s(x), each hole shifted proportionally to its position x along the axis, with shifts $s = 0$ and $s = s_{max}$ on each cavity termination, respectively. These linear shifts result in an approximately linear increase in the local effective index $n_{eff.}^{mode}$ of the waveguide or long-cavity confined modes, yielding cavity-confined modes with near field patterns and resonance frequencies that can be tailored by proper selections of s_{max}. The local effective index, referred to in Fig. 1 at a given position x along the cavity, corresponds to the effective index $n_{eff.}^{mode}$ of a uniform W_1 waveguide or a long L_n cavity of width $w + 2.s(x)$. The dot-dash line represents $n_{eff.}^{mode}$ for the unmodified uniform cavity structure of width w. The triangular "quantum well" thus formed confines optical modes with different photon energies E_0, E_1, ...

The mode patterns of such cavities (neglecting disorder and residual absorption) were simulated using a 2D finite difference method (FDM) [14]. Although 3D simulations would also provide a fair estimation of the modal Q-values, the real Q values are eventually limited by band-tail absorption and disorder (see experimental results below). Figure 2 displays the results for a triangular lattice PhC structure with pitch $a = 225$ nm, hole radius $r = 65.8$ nm and maximum hole shift $s_{max} = 20$ nm, based on a uniform L_{61} cavity fashioned in a GaAs membrane of thickness $t = 250$ nm. The calculated energy-position diagram (Fig. 2(a)) shows a series of confined modes, with a major peak of the spatial pattern (envelope function) increasingly shifted to the narrower end of the cavity (smaller x) for increasing mode energy. The envelope functions of the spatial mode distributions exhibit Airy-function like patterns [15], with the major lobe attached to a "tail" extending to larger values of x (Fig. 2(b)). The envelope functions of these Airy-Bloch modes are superposed on a periodic pattern (Bloch term) reflecting the periodicity of the base PhC structure. For a fixed value of s_{max} (or, equivalently, tilt of the effective index versus x), the main lobe of each mode is uniquely correlated with its energy, as denoted by the black and whites dashed lines in Fig. 2. Alternatively, the problem could be solved semi-analytically by employing the envelope-function formalism developed in [16]. By first simulating the bare GaAs slab dispersion, introduction of the W_1 PhC waveguide structure defines the guided waveguide bands arising from lateral confinement. Discretization of the bands into modes of a L_n cavity results from additional waveguide termination along x. Finally, modification into a tilted cavity recovers the Airy-Bloch confined modes. These unique mode patterns should be useful for, at the same time, efficient single photon extraction from a semiconductor QD placed at the major lobe and guiding it along the extended tail of the mode towards a detection path. Quite similarly to the trade-off required for a photon to leak from a cavity coupled to a waveguide channel, here a selection of the cavity tilt and specific Airy-Bloch mode would lead to compromise between sufficiently intense main lob and adequately long wavefunction tail.
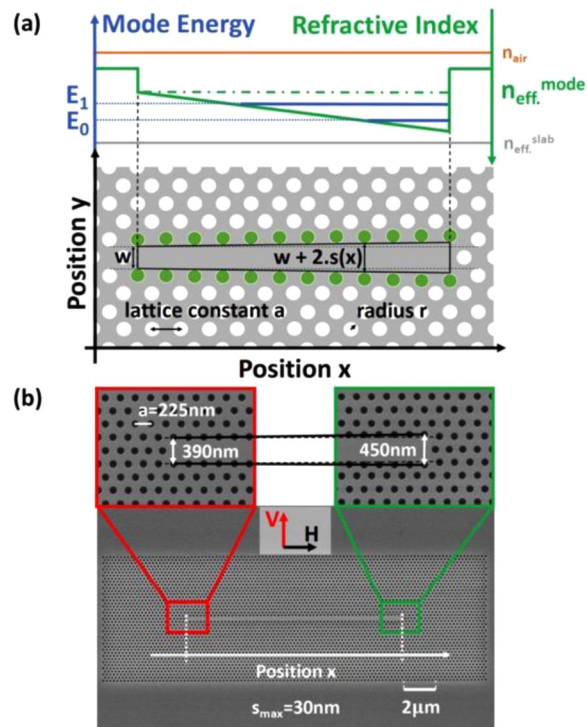
Fig. 1. (a) Schematic top-view illustration of the tilted-index GaAs membrane cavity (bottom) and its mode effective index variation, also showing the resonant mode energies (top). (b) Scanning electron microscope top-view images of a fabricated structure, with magnified view of the two cavity edges. Designed $s_{max}=30$ nm.
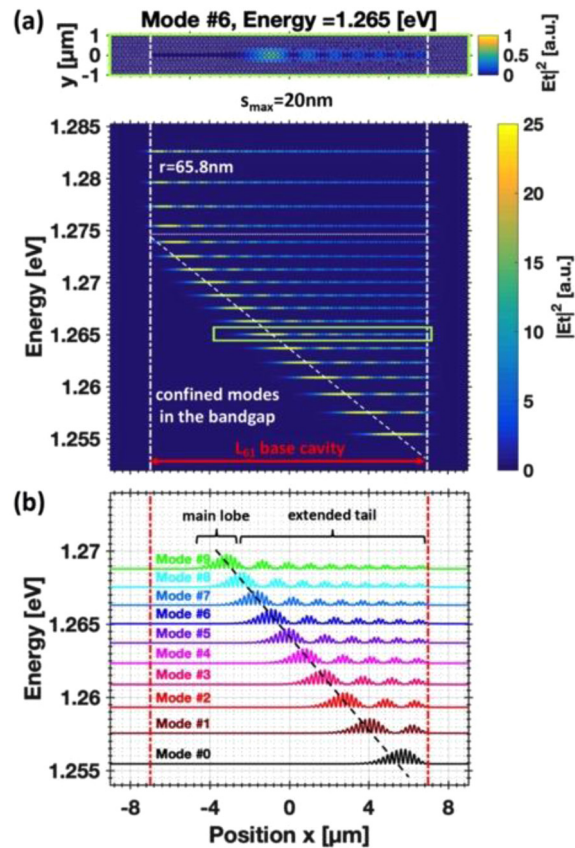
Fig. 2. Numerical simulation of the near-field intensity distributions of the lower-energy modes in a tilted-index cavity. (a) Energy-position plane presentation, with mode intensity integrated in the y-direction; upper panel shows the intensity distribution of the mode in frame in the x-y plane. (b) Spatial intensity along x of the first ten confined modes. Vertical dash-dot lines mark the left and right boundaries of the cavity. Parameters used: s_{max}=20 nm, pitch a = 225 nm, holes radii r = 65.8 nm, membrane thickness t = 250 nm, center effective index of slab $n_{eff.}^{slab}$=3.146. Dash-dot lines mark the edges of the cavity, dashed lines show linear approximations of the shifts of main lobe peak positions with mode energy.

3. Fabrication

The tilted-index cavities were fabricated in ∼250nm-thick GaAs membranes in which triangular arrays (450 nm pitch) of site-controlled InGaAs/GaAs QDs were incorporated [17], serving as integrated light sources or single photon emitters. The QDs were grown by organometallic vapor phase epitaxy [18,19] on arrays of etched pyramids of side length s_{pyr}∼255 ± 5 nm, emitting at λ_{QD}∼970-980 nm wavelength (∼1.27-1.28 eV energy) at T = 10 K [18]. The designed PhC hole patterns were implemented using electron beam lithography and inductive coupled plasma (ICP) dry etching, properly aligned with the QD arrays using special alignment marks [17]. The PhC holes were arranged on a triangular lattice of pitch a = 225 nm, designed for observing the confined modes in the 900-1000 nm wavelength range. Five groups of tilted-index structures, each consisting of 61 missing holes ($L_{n=61}$ configuration) along the cavity axis and with s_{max}=10, 15, 20, 25, or 30 nm, where integrated on the same sample. The shifts in holes were implemented in a step-wise fashion, with shifts of multiples of 1 nm (e.g., s_{max}=10 corresponds to 2 non-shifted holes and 10 groups of 6 holes shifted respectively by 1, 2, 3, up to 10 nm along the cavity axis). Numerical simulations confirmed that such lumped shifts do not change the essential effects we report, as compared with a smooth variation in hole positions. Each cavity type was repeated 21 times, systematically changing the PhC radius r from ∼50 to ∼70 nm in steps of 1 nm. The GaAs membranes, initially grown on a ∼1 μm thick sacrificial $Al_{0.7}Ga_{0.3}As$ layer on top of a (111)B GaAs substrate, were released at the last fabrication step using wet etching in a dilute HF solution.

4. Characteristics of Airy-Bloch modes

The Airy-Bloch modes, were observed by recording the photoluminescence (PL) patterns emitted by the structures under photo-excitation. In these experiments, we used structures in which an array of pyramidal QDs was aligned along the cavity axis (Fig. 2(a)), which permits to efficiently excite all modes confined by the cavity. The samples were illuminated at low temperature (10 K) by a continuous mode Ti:Sapphire laser beam at $\lambda_{exc.}$=730 nm wavelength (photo-excitation above the GaAs bandgap). The excitation spot was shaped into a ∼2 × 20μm^2 stripe using a 50X objective lens (NA = 0.55) and a cylindrical lens, for nearly uniform illumination of the entire cavity length. The spectrally resolved (diffraction-limited) near field of the photo-excited cavities was constructed by using an f = 30 cm lens to image the nearfield pattern on the entrance slit of a iHR550 spectrometer equipped by a 76mm*76 mm grating (1200grooves/mm, dispersion of 1.34 nm/mm) and dispersing it on its liquid N_2-cooled CCD camera (see [20] for more details). In this way, spectrally resolved near field patterns of the modes were acquired, with a spatial resolution of ∼1 μm and spectral resolution of ∼80μeV.

Figure 3 (center panel) shows the measured spectrally and spatially resolved images of the optical modes for fabricated structures with s_{max} = 10, 20, and 30 nm. The estimated values of the hole radii and s_{max} were based on SEM measurements on similar test structures fabricated during calibration runs. At the high excitation power employed ($P_{exc.}$=2 mW), each QD and its InGaAs barriers emit in a broad spectral range (∼830-1000 nm), permitting the excitation of all cavity modes spatially and spectrally overlapping with the light source. The measured patterns exhibit the typical Airy-Bloch mode patterns expected. Due to the finite spatial resolution, only the envelope functions of the modes are observed (i.e., the Bloch terms could not be resolved).

The simulated patterns corresponding to the measurements are also displayed in Fig. 3, excluding (left column) and including (right column) disorder effects. The hole radii employed were selected so as to fit the observed mode energies. The main features of the Airy-Bloch modes, particularly the principal and secondary ("tail") lobes, as well as the spectral and spatial distributions, are largely reproduced in the experiments for the larger potential slopes (s_{max}=20, 30 nm). A specific feature of the energy-position patterns is the virtually linear dependence of
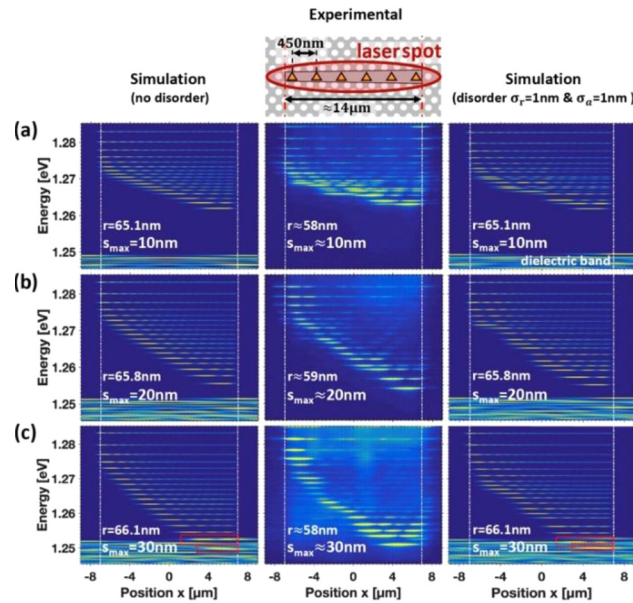
Fig. 3. Simulated and measured spectrally-resolved near-field patterns of tilted-index cavities with s_{max}=10, 20 and 30nm: simulated without disorder (left column); measured (center column); simulated with disorder (right column). Brightness scale for measured patterns corresponds to intensity (linear scales). Upper panel shows the experimental pumping arrangement. Dash-dot lines mark the left and right boundaries of the cavity. T = 10 K, excitation power (density) $P_{exc.}$=2 mW (~2.5 kW/cm^2).

the mode energy on the position of the main mode lobe, characterized by the slope dE/dx (see also Fig. 2). These slopes decrease systematically with decreasing values of s_{max}, with close agreement between experiment and modelling. This slope serves as a useful design parameter for tailoring the positions of the main lobes, hence the QDs eventually coupled to the modes, versus cavity resonance.

The Airy-Bloch mode patterns become significantly distorted for the smallest hole shift s_{max}=10 nm. In this case, the main intensity peak of each mode is not always located at the smallest x value, and the mode intensity is more randomly distributed along the cavity. These features are closely reproduced in the simulation by including fabrication-induce disorder in the form of random variations in hole radii and hole positions [20,21]. To simulate the disorder effects, we calculated the mode patterns assuming Gaussian distributions in hole radii and hole positions around their mean values, with standard deviations σ_r=1 nm and σ_a=1 nm, consistent with our previous studies of disorder in similar PhC structures [20]. For s_{max}=20 and 30 nm, such disorder is relatively weak, resulting in slight displacements of the mode energies and positions of the main mode lobes. On the other hand, for s_{max}=10 nm, the "deterministic" linear variation of the effective index along the cavity is too weak and the disorder introduces effective index variations that determine the mode energies and shapes. Interestingly, this analysis also serves as a tool for discerning the optical disorder in the system, via the observation of the minimum potential slope (or s_{max}) needed to impose the deterministic Airy-Bloch mode pattern on the mode structure.

More details on the observed Airy-Bloch modes are given in Fig. 4. The polarization-resolved, spatially integrated optical spectra shown in Fig. 4(a) display modes strongly polarized in the y-direction (see Fig. 1), exhibiting quality factors as large as 10'000. These values are not limited by the setup spectral resolution but rather by GaAs absorption bandtails and PhC disorder [22].

The spatial intensity patterns of the observed Airy-Bloch modes (envelope functions), directly extracted from the energy-space plots in Fig. 4(a), are displayed in Fig. 4(b). They are in good agreement with the near field patterns obtained from the numerical simulations.
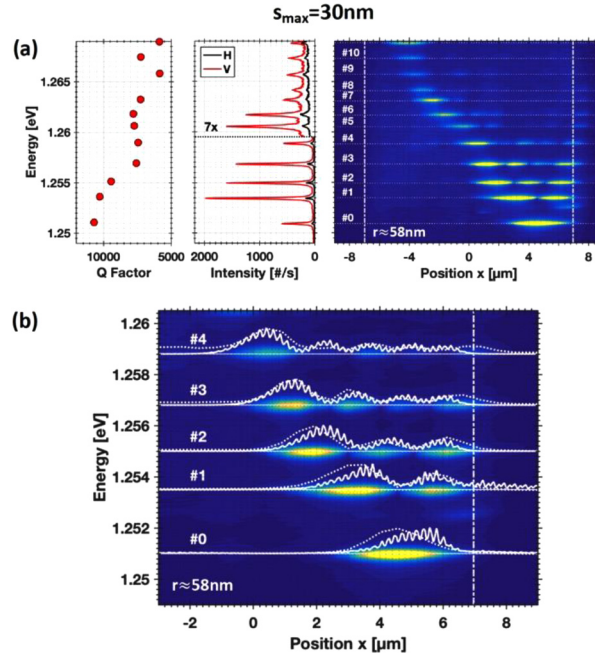

Fig. 4. Mode features of the tilted-cavity structure with s_{max}=30 nm (T = 10 K, $P_{exc.}$=2 mW (~2.5 kW/cm²). (a) Left panel: quality-factors and polarization-resolved spectra; right panel: enlarged spectrally and spatially resolved mode patterns. See Fig. 1 for definition of H- and V-polarizations. (b) Comparisons of measured and simulated near field patterns of the lowest energy Airy-Bloch modes. Image: measured spectrally-resolved intensity patterns. Dotted lines: measured (normalized) x-profiles obtained directly from the energy-position plots. solid line: normalized simulated near-field patterns, intensity integrated along the y-direction for r = 66.5 nm. Calculated modes are vertically shifted to fit mode energies.

The slope dE/dx, defined in terms of the energy E of a given Airy-Bloch mode and the position x of the envelope-peak of its main lobe, globally represents a particular tilted-potential cavity, and its value is important for designing the integration with arrays of site-controlled QDs. Figure 5 summarizes the slopes measured for several fabricated structures, and compares them with the results of numerical simulations. The experimental results are displayed only for s_{max} > 10 nm, as the smallest potential tilt do not produce mode patterns of well-defined dE/dx slopes (see Fig. 3). The simulations excluding disorder largely follow the measured results. The fabrication-induced disorder was modelled by introducing Gaussian distributions of the PhC hole positions and radii, with center values of r = 65 nm and a = 225 nm, and standard deviations of 1, 2 or 3 nm (10 statistical samples). The effect of disorder on the values of dE/dx is small but discernible. It should be noted that the calculated slope for the disorder-free structures with s_{max}=10 nm is significantly lower than the value expected from the linear fit to dE/dx for larger values of s_{max}. This deviation on slope occurs at dE/dx~1.3 meV/µm, which corresponds to a local variation of effective index of $dn_{eff}^{mode}/n_{eff}^{mode}$~dE/E~$10^{-3}$, which is another measure of the disorder-induced effective index fluctuations.
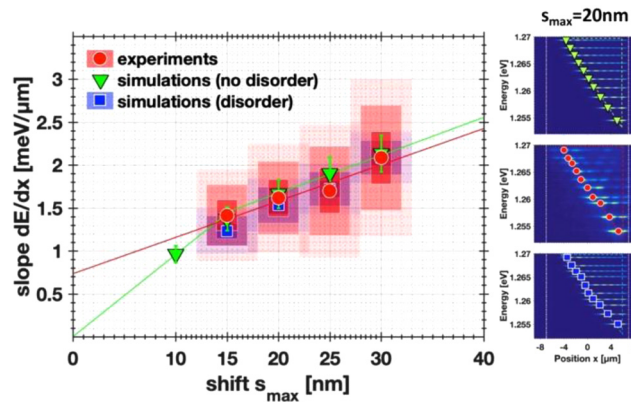
Fig. 5. Comparison of measured and simulated slopes dE/dx of the Airy-Bloch mode main lobe positions versus maximum hole shift s_{max}. Red circles: experiment; shaded areas correspond to the statistical 1, 2, and 3σ variations of slopes measured from several structures and $\pm 1, 2, 3$ nm uncertainty in actual s_{max} values. Blue squares: simulations including disorder; shaded areas correspond to the statistical 1, 2, 3 variations e of slopes extracted from simulations including both $\sigma_r=1$ nm and $\sigma_a=1$ nm for Gaussian distributions of hole radii and positions. Solid lines are linear fits to the corresponding symbols. Green triangles: slope values extracted from simulations without disorder; error bars correspond to 10% percent uncertainty in parameters. Solid green lines: linear for $s_{max}=10$-15 nm and $s_{max}=15$-30 nm. Right column: energy-position mode patterns of selected corresponding measurements and simulations indicating the main lobe positions; $s_{max}=20$ nm.

5. Selective Airy-Bloch mode excitation

The peculiar mode patterns of the tilted-index structures allow selective excitation of a particular Airy-Bloch mode using a properly positioned, site-controlled light source. This can be accomplished with site-controlled QDs, thus permitting the transfer of the extracted single photons along the tilted-index cavity to a prescribed destination. Such integration of a QD with a tilted-potential cavity is useful for optimizing the required mode intensity distribution: peaked intensity at the QD site for enhancing the Purcell effect, and a delocalized wavefunction tail for efficient photon transfer.

Such selective Airy-Bloch mode excitation was implemented by fabricating tilted-index cavities with single pyramidal QDs located at specific positions along the cavities. A particular configuration employed is depicted schematically at the top of Fig. 6. The structure incorporates two pyramidal InGaAs/GaAs dots, QD_A and QD_B, separated by sufficiently large distance to allow their individual optical excitation by the focused laser beam. The alignment precision of the QDs with respect to the cavity is better than 50 nm, achieved using proper alignment marks in the electron beam lithography processes involved [17].

Figure 6 demonstrates Airy-Bloch mode selective excitation using a system of two InGaAs/GaAs pyramidal QDs, positioned at x=−3.4μm and + 6.1μm (see scale in Fig. 1; x = 0 is at the cavity center). For the specific structure shown, $s_{max}=20$ nm and r≈58 nm. The QDs are grown in pyramids of the same nominal size (pyramid side $s_{QD}\sim243 \pm 5$ nm), emitting from the ground s-states around $\lambda_{QD}\sim980$-990 nm (~1.25-1.27 eV) at T = 10 K. The stripe geometry of the exciting laser spot provides simultaneously localized light sources at two specific positions along the cavity. At high excitation power of $P_{exc.}=2$ mW (2.5 kW/cm²) (Fig. 6(a)), each QD emits in broad band through excited and barrier states and tails, exciting preferentially the Airy-Bloch modes with the main lobes at the QD positions. Comparison with the calculated Airy-Bloch mode patterns (white curves in Fig. 6) allows the identification of the modes that are selectively
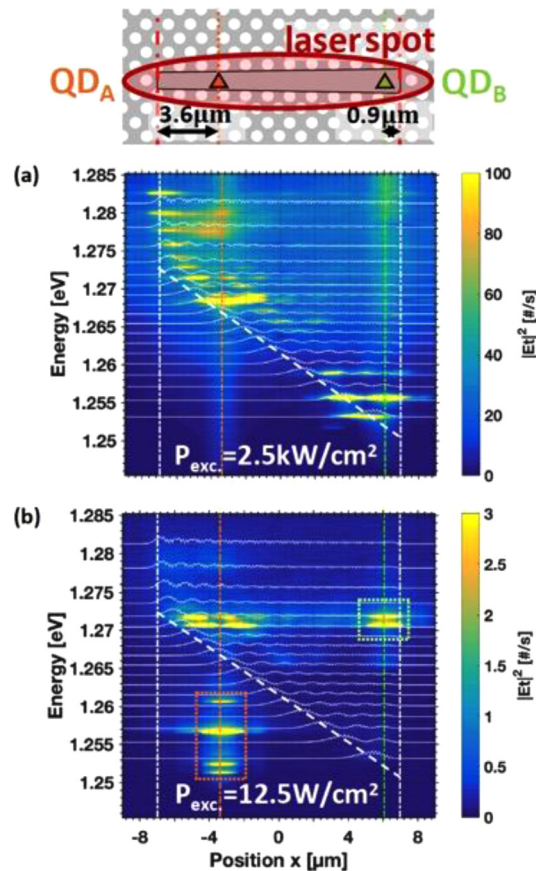
Fig. 6. Selective excitation of Airy-Bloch modes using single, site-controlled QDs placed at specific positions along the tilted-index cavities (s_{max}=20 nm, r≈58 nm). Upper panel: schematics illustration of the cavity-QD system. (a) and (b): energy-position plots of mode patterns for $P_{exc.}$=2 mW (~2.5 kW/cm^2) and $P_{exc.}$=10μW (~12.5W/cm^2). T = 10 K. White curves show simulated Airy-Bloch modes (s_{max}=20 nm, r = 65.2 nm, t = 250 nm, $n_{eff.}^{slab}$=3.14, no disorder). Vertical orange and green dash-dot lines mark positions of the two QDs. Dashed orange and green boxes specify the s-shell emissions of, respectively, QD_A and QD_B.

excited. The single-QD nature of the light sources is revealed by examining the patterns at much lower excitation level ($P_{exc.}$=10μW (12.5W/cm^2), displayed in Fig. 6(b). At this low excitation, the emission spectrum exhibits sharp, localized emission lines related to the s- and p-states of the QDs. The difference in emission energies of QD_A and QD_B is a result of the inhomogeneous broadening of the emission of the QD ensemble. The p-state transitions of QD_A feed the excitation of the higher order Airy-Bloch states localized at the left-hand part of the cavity. On the other hand, the s-state transitions of QD_B emit at energy higher than the energy of the Airy-Bloch modes localized at its position, and hence cannot excite any cavity mode. Several design parameters are available for achieving resonant coupling between the QD emission spectra and the Airy-Bloch modes: the PhC hole radii for shifting the mode energies as a whole, the size of the pyramids used for growing the QDs for shifting their emission spectra [18,19], and the value of s_{max} for adjusting slope dE/dx and thus the mode dispersion. Eventual fine tuning can

be accomplished via temperature variation [23,24] or applications of electric [25] or strain [26] fields.

6. Conclusion

In conclusion, we proposed and demonstrated tilted-index PhC membrane cavities that confine Airy-Bloch optical modes. These modes are unique in two respects. First, their spatial patterns are highly non-uniform. They exhibit both a localized part and an extended, delocalized tail, allowing efficient single photon extraction and transport to a remote location when properly coupled to a site-controlled QD. One example of a specific use is the integration of a grating coupler to the end of the cavity (extended tail side), which would couple the photons into free space as readily done with uniform cavities and waveguides [12]. Second, the group of Airy-Bloch modes displays a characteristic dispersion of their energy versus the location of their main-localized lobe, represented by the slope dE/dx defines and analyzed above. This feature allows the design of multiple-QD systems emitting at prescribed wavelengths, coupled collectively to the tilted-index cavity. The high-precision site-control of the pyramidal QDs is a natural outcome of their growth in lithographically-defined pyramidal pattern. The control on their emission wavelength stems from the controlled dependence of their growth rate on the size of the pyramidal recess [18,19]. More generally, integrating site- and energy-controlled QD systems with such tilted-index cavities would permit the generation and on-chip routing of single photons for applications in integrated quantum photonics.

Appendix

The optical modes of the tilted-potential photonic crystal (PhC) cavities were simulated numerically using a 2D finite difference method [14]. First, the effective index $n_{eff.}^{slab}$ of the uniform GaAs suspended membrane was calculated, using the estimated membrane thickness, at the measurement temperature and for the membrane thickness. The value for the GaAs refractive index [27] was selected for the approximate wavelength at which the confined modes were expected (around 980 nm). The 2D PhC hole pattern was then simulated in the form of air-holes of uniform radii r on a perfect triangular lattice of pitch a, except for those surrounding the cavity, as described in the main text. The confined modes were calculated for each tilted-potential cavity configuration, i.e., the specific number of removed-holes and maximum shift s_{max}.

Next, to account for the dispersion of the refractive index of GaAs n_{GaAs}, the effective index of the membrane was recalculated for the wavelength of the tilted-potential mode at the center of the Airy-Bloch mode group ("center mode") found in the initial approximation. The entire set of the Airy-Bloch modes was then recalculated for this corrected value of $n_{eff.}^{slab}$. At this stage, the energy of the center mode almost perfectly matched (within less than ~100μeV) the photon energy for which n_{GaAs} was set. At the subsequent steps, the effective index of the membrane was corrected successively for each mode around the center mode, such that improved mode resonances were obtained for all simulated modes. The entire energy-position pattern was finally constructed using the thus corrected images for each individual mode. This procedure yielded a mode patterned with energies consistent with the wavelength dispersion of GaAs, with maximum error of 100μeV. An example of such simulation is given in Fig. 5 (green triangles in left panel and top image on right column).

In the article, all other simulated Airy-Bloch mode patterns were calculated using a simplified approach. After simulating the mode pattern with the refractive index n_{GaAs} calculated at wavelength λ_0 yielding an accurate value of the energy $E^{(0)}(\lambda_0)$ of the center mode, we estimated the correction ΔE in the energy of a neighboring mode E using the relationship

$$\frac{\Delta E}{E} \approx -\frac{\Delta n_{eff.}^{slab}}{n_{eff.}^{slab}}, \qquad (1)$$

accounting for the change $\Delta n_{eff.}^{slab}$ in the effective membrane index due to the shift in the resonance wavelength (at λ) with respect to the center mode. Thus, starting with the first-order approximation for a mode energy

$$E^{(correct.)}(\lambda) \approx E^{(0)}(\lambda_0) - \left(\frac{n_{eff.}^{slab}(\lambda) - n_{eff.}^{slab}(\lambda_0)}{n_{eff.}^{slab}(\lambda_0)} \right) \cdot E^{(0)}(\lambda_0). \tag{2}$$

The accuracy of this approximation was checked by comparing the calculated resonances using the iterations described above and this simplified approach. We find that the approximation yields resonance energies that agree within ~1.2 meV across the entire band of the Airy-Bloch modes discussed in the article.

Funding

Acknowledgment

References

1. D. Englund, D. Fattal, E. Waks, G. Solomon, B. Zhang, T. Nakaoka, Y. Arakawa, Y. Yamamoto, and J. Vučković, "Controlling the spontaneous emission rate of single quantum dots in a two-dimensional photonic crystal," Phys. Rev. Lett. **95**(1), 013904 (2005).
2. M. Arcari, I. Söllner, A. Javadi, S. Lindskov Hansen, S. Mahmoodian, J. Liu, H. Thyrrestrup, E. Lee, J. Song, S. Stobbe, and P. Lodahl, "Near-Unity Coupling Efficiency of a Quantum Emitter to a Photonic Crystal Waveguide," Phys. Rev. Lett. **113**(9), 093603 (2014).
3. J. L. O'Brien, A. Furusawa, and J. Vučković, "Photonic quantum technologies," Nat. Photonics **3**(12), 687–695 (2009).
4. S. F. Poor, T. Hoang, L. Midolo, C. Dietrich, L. Li, E. Linfield, J. Schouwenberg, T. Xia, F. Pagliano, F. Van Otten, and A. Fiore, "Efficient coupling of single photons to ridge-waveguide photonic integrated circuits," Appl. Phys. Lett. **102**(13), 131105 (2013).
5. H. P. Seigneur, M. Weed, M. N. Leuenberger, and W. V. Schoenfeld, "Controlled On-Chip Single-Photon Transfer Using Photonic Crystal Coupled-Cavity Waveguides," Adv. OptoElectron. **2011**, 1–13 (2011).
6. D. Sahin, A. Gaggero, Z. Zhou, S. Jahanmirinejad, F. Mattioli, R. Leoni, J. Beetz, M. Lermer, M. Kamp, S. Höfling, and A. Fiore, "Waveguide photon-number-resolving detectors for quantum photonic integrated circuits," Appl. Phys. Lett. **103**(11), 111116 (2013).
7. P. Lodahl, S. Mahmoodian, and S. Stobbe, "Interfacing single photons and single quantum dots with photonic nanostructures," Rev. Mod. Phys. **87**(2), 347–400 (2015).
8. R. Konoike, H. Nakagawa, M. Nakadai, T. Asano, Y. Tanaka, and S. Noda, "On-demand transfer of trapped photons on a chip," Sci. Adv. **2**(5), e1501690 (2016).
9. C. P. Dietrich, A. Fiore, M. G. Thompson, M. Kamp, and S. Höfling, "GaAs integrated quantum photonics: Towards compact and multi-functional quantum photonic integrated circuits," Laser Photonics Rev. **10**(6), 870–894 (2016).
10. A. Faraon, E. Waks, D. Englund, I. Fushman, and J. Vučković, "Efficient photonic crystal cavity-waveguide couplers," Appl. Phys. Lett. **90**(7), 073102 (2007).
11. D. Englund, A. Faraon, B. Zhang, Y. Yamamoto, and J. Vučković, "Generation and transfer of single photons on a photonic crystal chip," Opt. Express **15**(9), 5550–5558 (2007).
12. B. Rigal, B. Dwir, A. Rudra, I. Kulkova, A. Lyasota, and E. Kapon, "Single photon extraction and propagation in photonic crystal waveguides incorporating site-controlled quantum dots," Appl. Phys. Lett. **112**(5), 051105 (2018).
13. B. Rigal: *Thesis 8304: Site-controlled quantum dots integrated with photonic crystal waveguides and cavities* (EPFL, 2018).
14. K. A. Atlasov, M. Felici, K. F. Karlsson, P. Gallo, A. Rudra, B. Dwir, and E. Kapon, "1D photonic band formation and photon localization in finite-size photonic-crystal waveguides," Opt. Express **18**(1), 117–122 (2010).
15. L. Landau and E. Lifshitz, *Quantum Mechanics: Non-Relativistic Theory* (Addison-Wesley, 1958).
16. M. Charbonneau-Lefort, E. Istrate, M. Allard, J. Poone, and E. H. Sargent, "Photonic crystal heterostructures: Waveguiding phenomena and methods of solution in an envelope function picture," Phys. Rev. B **65**(12), 125318 (2002).

17. P. Gallo, M. Felici, B. Dwir, K. A. Atlasov, K. F. Karlsson, A. Rudra, A. Mohan, G. Biasiol, L. Sorba, and E. Kapon, "Integration of site-controlled pyramidal quantum dots and photonic crystal membranes cavities," Appl. Phys. Lett. **92**(26), 263101 (2008).

18. I. V. Kulkova, A. Lyasota, C. Jarlov, B. Rigal, A. Rudra, B. Dwir, and E. Kapon, "Emission wavelength control of ordered arrays of InGaAs/GaAs quantum dots," J. Cryst. Growth **464**, 69–74 (2017).

19. A. Surrente, M. Felici, P. Gallo, A. Rudra, B. Dwir, and E. Kapon, "Dense arrays of site-controlled quantum dots with tailored wavelength: Growth mechanisms and optical properties," Appl. Phys. Lett. **111**(22), 221102 (2017).

20. B. Rigal, D. Drahi, C. Jarlov, B. Dwir, A. Rudra, I. Kulkova, A. Lyasota, and E. Kapon, "Probing disorder and mode localization in photonic crystal cavities using site-controlled quantum dots," J. Appl. Phys. **123**(4), 043109 (2018).

21. V. Savona, "Electromagnetic modes of a disordered photonic crystal," Phys. Rev. B **83**(8), 085301 (2011).

22. B. Rigal, K. Joanesarson, A. Lyasota, C. Jarlov, B. Dwir, A. Rudra, I. Kulkova, and E. Kapon, "Propagation losses in photonic crystal waveguides: effects of band tail absorption and waveguide dispersion," Opt. Express **25**(23), 28908 (2017).

23. A. Faraon and J. Vučković, "Local temperature control of photonic crystal devices via micron scale electrical heaters," Appl. Phys. Lett. **95**(4), 043102 (2009).

24. S. Sokolov, J. Lian, E. Yüce, S. Combrié, A. De Rossi, and A. P. Mosk, "Tuning out disorder-induced localization in nanophotonic cavity arrays," Opt. Express **25**(5), 4598–4606 (2017).

25. T. B. Hoang, J. Beetz, M. Lermer, L. Midolo, M. Kamp, S. Höfling, and A. Fiore, "Widely tunable, efficient on-chip single photon sources at telecommunication wavelength," Opt. Express **20**(19), 21758–21765 (2012).

26. S. Sun, H. Kim, G. S. Solomon, and E. Waks, "Strain tuning of a quantum dot strongly coupled to a photonic crystal cavity," Appl. Phys. Lett. **103**(15), 151102 (2013).

27. S. Gehrsitz, F. K. Reinhart, C. Gourgon, N. Herres, A. Vonlanthen, and H. Sigg, "The refractive index of $Al_xGa_{1-x}As$ below the band gap: Accurate determination and empirical modeling," J. Appl. Phys. **87**(11), 7825–7837 (2000).